Piezocatalytic oxidation of 5-hydroxymethylfurfural to 5-formyl-2-furan-carboxylic acid over Pt decorated hydroxyapatite

Zhiwei Chen, Hongru Zhou, Fanhao Kong, Min Wang [*]

Zhang Dayu School of Chemistry, Dalian University of Technology, Dalian 116024, Liaoning, China

A B S T R A C T

Selective oxidation of 5-hydroxymethylfurfural (HMF) to 5-formyl-2-furancarboxylic acid (FFCA) is a critical reaction for producing value-added chemicals from biomass. The challenge for this reaction is to develop an efficient catalytic process that can be conducted under mild conditions. Herein, we first propose piezocatalytic HMF oxidation using a Pt decorated hydroxyapatite (HAP) piezocatalyst (Pt/HAP). The introduction of Pt on HAP creates an interfacial electric field. The couple of nonlocal piezoelectric field and localized interfacial electric field greatly promotes both the bulk and surface charges transfer. Moreover, Pt not only promotes the separation of piezo-induced charges but also activates oxygen molecules and organic functional groups of the substrates. Compared with pristine HAP, Pt/HAP exhibits outstanding piezocatalytic activity, which reached 96% HMF conversion and 70% FFCA yield in 2 h under room temperature. A wide range of aldehydes and alcohols, such as fatty aldehydes, furan aldehydes, fatty alcohols, and ethylene glycol, were all oxidized to carboxylic acids. This work provides a novel method on utilizing piezocatalysis for biomass conversion.

1. Introduction

Biomass is the only promising renewable non-fossil-based carbon resource with advantages of abundant reserves, easy accessibility, and utilization without changing the current carbon balance of the ecosystem [1–6]. 5-Hydroxymethyl-furfural (HMF), the dehydration product of C6 carbohydrates, is regarded as an important platform molecule to produce various high-value-added chemicals [7,8]. HMF possesses two functional groups, the alcoholic group and the aldehydic (-CH$_2$OH and -CHO). The oxidation of HMF could produce 2,5-diformyl-furan (DFF), 5-hydroxymethyl-2-furancarboxylic acid (HMFCA), 5-formyl-2-furancarboxylic acid (FFCA), 2,5-furancarboxylic acid (FDCA). Over the past decades, much research has been focused on the oxidation of HMF to DFF, HMFCA and FDCA with a great success [9–11]. However, the oxidation of HMF to 5-formyl-2-furancarboxylic acid (FFCA), which possesses two functional groups (-CHO and -COOH) and exhibits considerable potential in medicine and furan-based polyesters [12,13], was rarely reported. The deep oxidation to one carboxylic (-COOH) group while prohibiting one aldehydic group (-CHO) deep oxidation makes the selective production of FFCA difficult. The catalytic oxidation of HMF to FFCA was reported at elevated temperatures and high oxygen pressure but with low activity in the air [14]. Enzyme catalysis realized

the mild oxidation of HMF to FFCA but with the short process-life and instability of enzymes [15]. Therefore, developing new routes for high-efficiency transformation from HMF to FFCA under mild conditions is still a challenging target.

Recently, piezocatalysis driven by mechanical energies (such as sonic waves, tide, wind, and atmospheric pressure) has attracted widespread attention [16–21]. The piezo-potential induced by stress can induce a giant electric field, which drives the separation and migration of electrons and holes to participate in the surface reaction under mild conditions. Piezoelectric-based catalysis relies on the charge separation efficiency. Compared with photo-driven charges separation [22], stress-induced charge carriers show much lower efficiency. The couple of piezocatalysis and photocatalysis, namely piezo-photocatalysis, was generally employed to improve the efficiency [23]. Up to now, some successes have been achieved on the piezocatalytic degradation of organic pollutions and water splitting [24–26], while either piezocatalysis or piezo-photocatalysis has never been realized in biomass conversion to produce valuable chemicals.

Herein, we first propose a novel piezocatalytic approach toward the selective oxidation of HMF into FFCA. Hydroxyapatite (Ca$_{10}$(PO$_4$)$_6$(OH)$_2$, HAP), whose piezoelectricity originates from the ferroelectric ordering of the OH$^-$ ions along the [001] direction, was

---
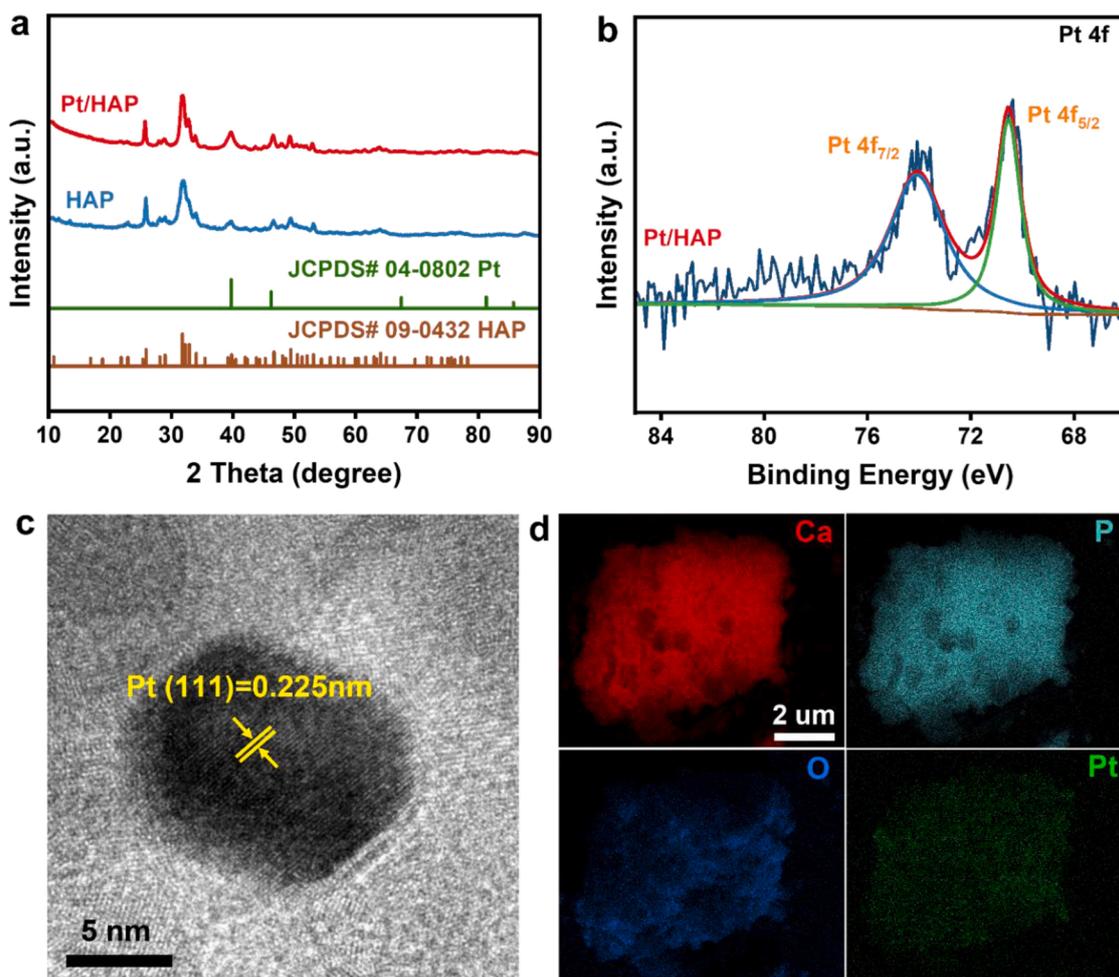
Fig. 1. (a) The XRD patterns of HAP and Pt/HAP. (b) High-resolution XPS spectra of Pt 4f. (c) HRTEM image of Pt/HAP. (d) Elemental mapping images of Pt/HAP.

used as the piezoelectric materials [27–29]. Pt nanoparticles were loaded on the HAP to construct an interfacial electric field and thus boost stress-induced charges separation. Moreover, Pt could effectively active O_2 molecules and organic functional groups of the substrates. Compared with HAP, Pt/HAP catalyst improves catalytic activity, showing 96% HMF conversion and 70% FFCA yield in the air under ultrasonic vibration at ambient temperatures while pristine HAP was nearly inactive. This work will provide new inspirations on utilizing mechanical energies for biomass conversion.

2. Experimental section

2.1. Reagents

All commercial chemicals of analytical grade were used without further purification. 5-Hydroxymethylfurfural (HMF) , 5-hydroxymethyl-2-furancarboxylic acid (HMFCA), 5-formyl-2-furancarboxylic acid (FFCA) and 2,5-furan dicarboxylic acid (FDCA) were purchased from Aladdin Industrial Corporation. The commercial HAP was purchased from Shanghai Aladdin Bio-Chem Technology Co., Ltd. (Item No. H106378). HNO_3, methanol, 4-benzoquinone (BZQ) and isopropanol (IPA) were purchased from Tianjin Kermel Chemical Reagent Co. Ltd. Bi $(NO_3)_3 \cdot 5H_2O$, Na_2WO_4, NaOH, KIO_3, $CaCl_2$, $CuCl_2$, $(NH_4)_2HPO_4$, CH_3CH_2OH, HCOOH, CH_3COOH, HCHO, CH_3CHO, $CH_3CH_2CH_2OH$, CH_3CH_2CHO, CH_3CH_2COOH were purchased from Tianjin Damao Chemical Reagent Factory. Furfural, furan carboxylic acid, 5-Bromo-2-furaldehyde, 5-Bromofuran-2-carboxylic acid, ethylene glycol, and glycol acid were purchased from Innochem Chemical Reagent Co. Ltd.

$HAuCl_4 \cdot 4H_2O$, $H_2PtCl_6 \cdot 6H_2O$, $IrCl_3 \cdot xH_2O$ and $RuCl_3 \cdot xH_2O$ were purchased from CNMC Shenyang Research Institute of Nonferrous Metals. Water was purified using a Millipore Milli- 57Q Advantage A10 water purification system to a resistivity higher than 18 MΩ.cm. Ar (>99.999%) and H_2 (>99.999%) were provided by Dalian Junfeng Gas Chemicals Co. Ltd.

2.2. Catalyst preparation

The HAP-supported catalyst with 3 wt% weight of metal was prepared by the impregnation method. Typically, 0.5 g commercial HAP was dispersed in 20 mL deionized water with a certain volume of H_xMCl_y mH_2O solution. After stirring for 24 h, the mixture was placed on a 150 ºC heating plate to evaporate the water. The obtained powder was then reduced at 400 ºC by H_2 (20 mL·min^{-1}) for 3 h with a ramp rate of 2 ºC min^{-1}. The above catalysts were named Au/HAP, Rh/HAP, Ir/HAP, and Pt/HAP.

2.3. Characterization

X-ray diffraction (XRD) patterns were recorded on Bruker D8 Advance (Cu Kα = 1.5404 Å) to analyze the phase and structure with a scanning rate of 0.05° s^{-1} from 10° to 90°. Transmission electron microscope (TEM) and high-resolution transmission electron microscopy (HRTEM) were measured on a JEOL 2100-F (JEOL, Japan) microscope with an accelerating voltage of 200 kV. X-ray photoelectron spectroscopy (XPS) was recorded on a VG Multi lab 2000 (VG Inc.) photoelectron spectrometer using monochromatic Al Kα radiation as the excitation
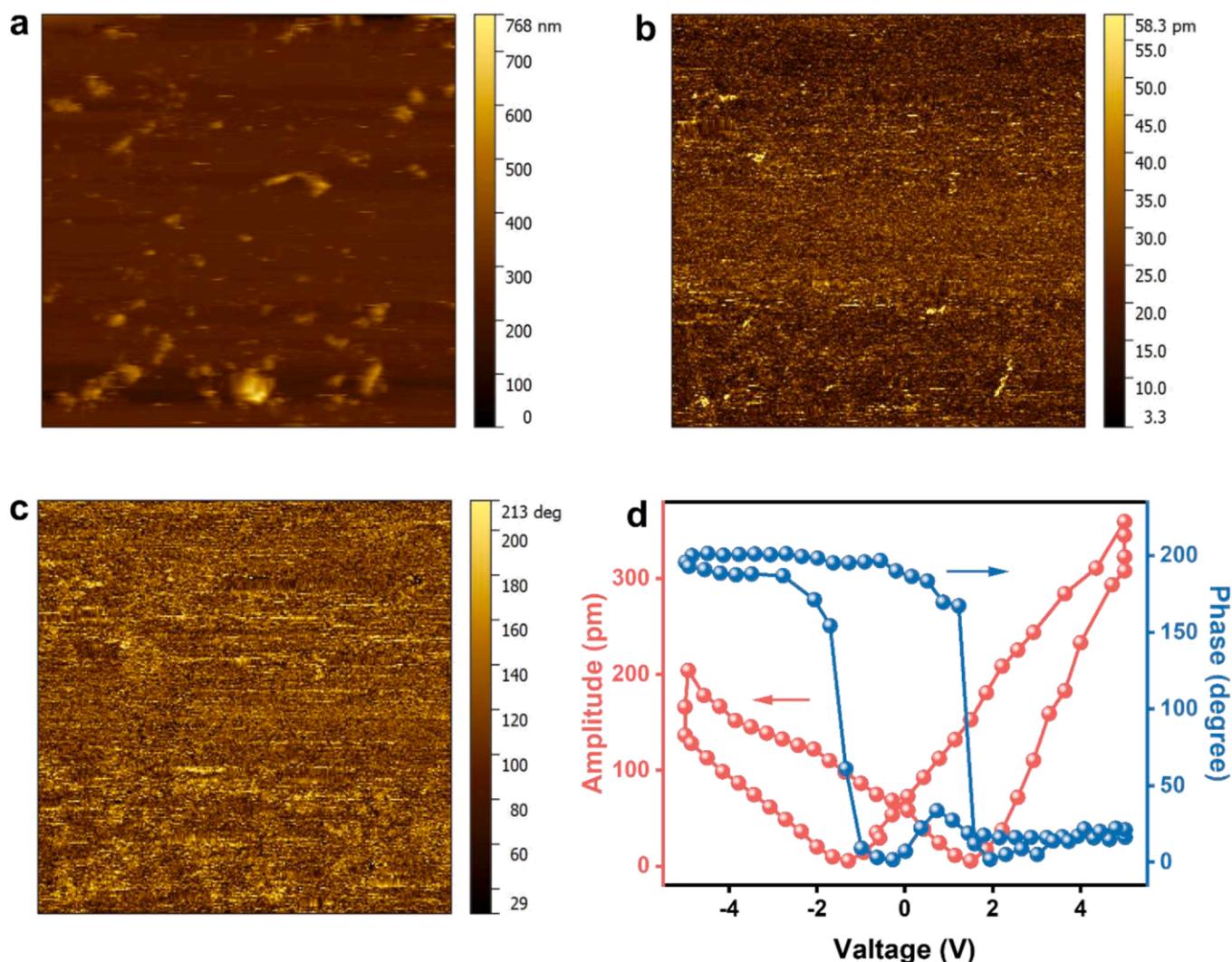
Fig. 2. PFM images of Pt/HAP. (a) Topography. (b) Amplitude. (c) Phase. (d) Amplitude butterfly and phase hysteresis loops.

source under vacuum at 2×10^{-6} Pa. The charged correction of binding energy was conducted with the C 1 s = 284.80 eV. Energy Dispersive X-ray Spectroscopy (EDS) was conducted on SU8010 field-emission scanning electron microscope (FESEM, Hitachi, Japan). UV–vis diffuse reflectance spectra (UV–vis DRS) were recorded on a UV–vis spectro-photometer (Agilent UV-550) at room temperature in the range of 200–800 nm with $BaSO_4$ as the background. The electron paramagnetic resonance (ESR) experiment was conducted on a Bruker spectrometer at X-band under room temperature with a field modulation of 100 kHz.

The formaldehyde adsorption FTIR spectra were recorded using a Thermo Scientific Nicolet iS10 IR spectrometer. PFM measurements were done upon a Bruker Dimension ICON atomic force microscope (AFM) equipped with a ferroelectric test system; the Pt/HAP suspension was spin-coated onto a Pt deposited $SrTiO_3$ substrate. During the PFM characterization, the AC bias for the measure in amplitude and phase images was 0 V, and the resonance frequency for measuring the butterfly-shaped amplitude curve and the hysteresis loop was 275.5 kHz. The ferroelectric property of Pt/HAP was studied by a ferroelectric analyzer (aixACCT TF-2000E) at 8000 mV and 1 Hz under room temperature. The Pt/HAP sample was pressed in a tablet (diameter of∼ 10 mm and thickness of ∼ 1 mm) without further annealing, then silver paste was applied to both sides of the tablet (effective area of ∼30 mm^2). Electrochemical tests were conducted in an Autolab (PGSTAT302N) workstation with a conventional three-electrode cell system: both the working electrode and the counter electrode were Pt sheets and a

saturated calomel electrode was used as the reference electrode. 30 mg of HAP or Pt/HAP was dispersed in 30 mL of 0.5 mol L^{-1} Na_2SO_4 electrolyte. The Mott-Schottky plot of HAP or Pt/HAP was taken at a frequency of 1 kHz. It should be noted that the direction of the current (positive or negative) depended on the open circuit potential, which was positive during the analysis and likewise the current response.

2.4. Piezocatalytic HMF oxidation

Piezocatalytic experiments were conducted in a cylindrical jacketed Teflon reactor. Ultrasonic irradiation was provided by an ultrasonic generator (Xi 'an Taikang, China), equipped with a titanium probe transducer that emits ultrasound waves at 20 kHz and provides a set power output of 400 W. An ultrasonic probe with a tip diameter of 10 mm was inserted into the solution at a depth of 6 cm without touching the bottom of the Teflon reactor. The sonication was performed in a pulse mode of 3.0 s On and 2.0 s Off. Typically, 50 mg Pt/HAP catalysts, 3.2 mmol L^{-1} HMF, and 10 mL deionized water were added into the reactor under air atmosphere for 2 h. After the reaction, a transparent solution was obtained by using a 0.22 μm organic filter membrane, which was further analyzed on HPLC.

2.5. HPLC analysis

A high-performance liquid chromatography (HPLC, Shimadzu
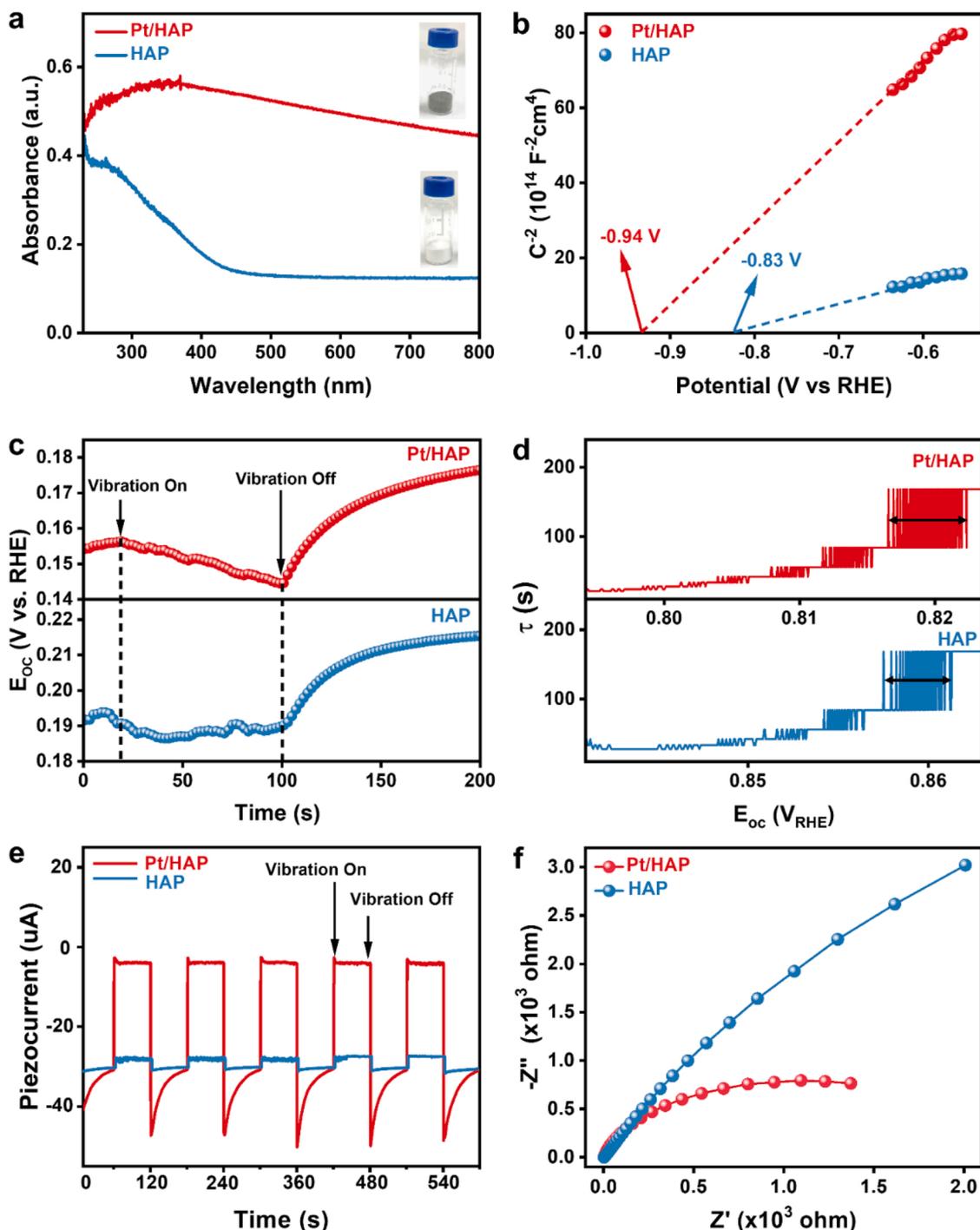
Fig. 3. (a) DRS spectrum. (b) Mott-Schottky plots. (c) Transient open-circuit voltage decay (OCVD) curves. (d) The average lifetime distribution of piezo-induced charge carrier. (e) Transient piezocurrent response under the vibration. (f) Electrochemical impedance spectroscopy (EIS).

Prominence LC-20 CE) with an ultraviolet-visible detector (265 nm) and an XBridge C18 column (4.6 mm × 150 mm, 5 μm) was used to analyze the concentration of HMF and its oxidation product. The mobile phase was V(H$_2$SO$_4$, 0.05 wt%):V(CH$_3$OH) = 80:20 with a flow rate of 0.5 mL/min, and the column temperature was 40 ℃. Sample solutions (30 μL) were diluted with 1.47 mL of 0.05 wt% H$_2$SO$_4$, and 10 μL of a diluent was injected using an autosampler. The calibration curves of pure HMF, HMFCA, FFCA, and FDCA standard solutions were further recorded to quantify the HMF conversion and HMFCA, FFCA, and FDCA yield. Conversion of HMF, the yield of HMFCA, FFCA, and FDCA were calculated as follows:

HMF Conversion (%) = [n(HMF consumed)/n(HMF initial)] × 100%.
HMFCA Yield (%) = [n(HMFCA)/n(HMF initial)] × 100%.
FFCA Yield (%) = [n(FFCA)/n(HMF initial)] × 100%.
FDCA Yield (%) = [n(FDCA)/n(HMF initial)] × 100%.

n(HMF consumed) is the molar amount of consumed HMF during the reaction and n(HMF initial) is the initial molar amount of HMF. n(HMFCA), n(FFCA) and n(FDCA) represent the molar of HMFCA, FFCA and FDCA, respectively.
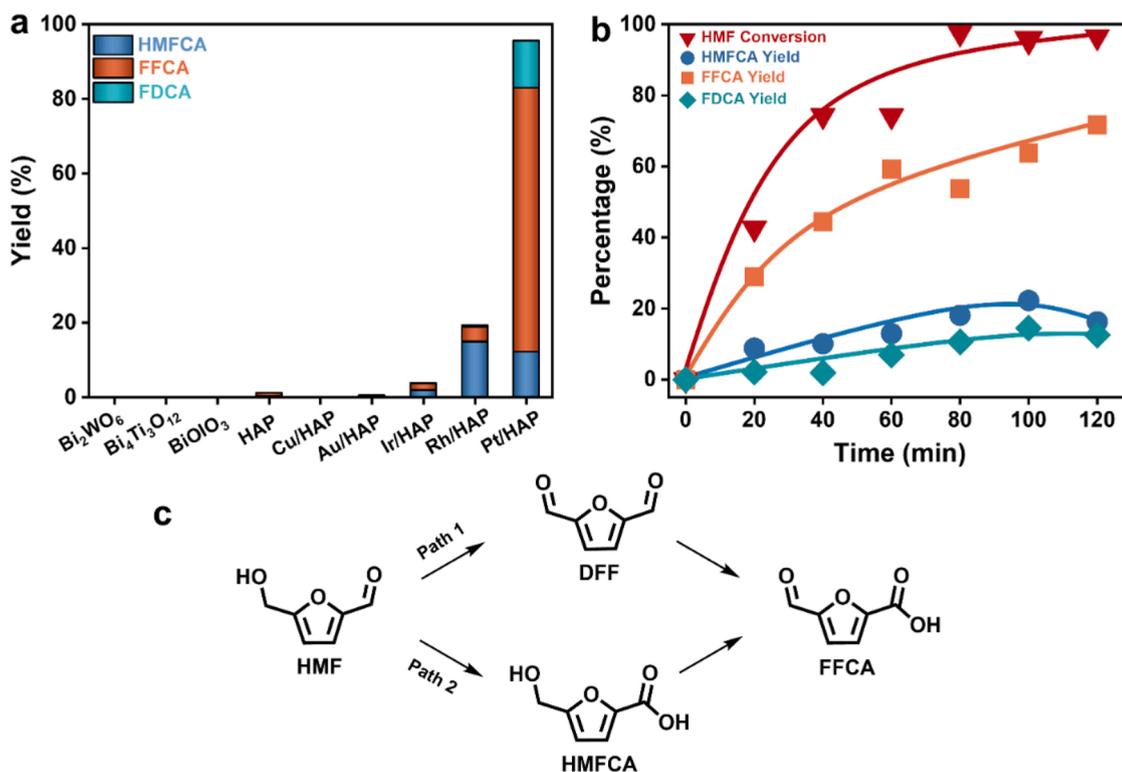
Fig. 4. (a) Piezocatalytic HMF oxidation over various catalysts. Reaction conditions: 10 mL of HMF aqueous solution (3.2 mmol L^{-1}), 50 mg of catalysts, 1 atm air, 2 h. (b) Time curve of HMF oxidation. (c) Two possible pathways of HMF oxidation to FFCA.

Table 1
Piezocatalytic oxidation of aldehydes and alcohols.

Entry	Substrate	Product	Conversion / %	Yield / %
1			71	62
2			89	84
3			96	78
4			66	46
5			62	54
6			65	43
7			77	68
8			83	68
9			58	47

Reaction conditions: 10 mL of substrate aqueous solution (3.2 mmol L^{-1}), 50 mg of Pt/HAP, 1 atm air, 4 h.

2.6. DFT calculation

All of the first-principles electronic structure calculations were carried out using the Vienna ab initio simulation package (VASP) [30], one density functional theory implementation. The exchange-correlation potential was described by the Perdew–Burke–Ernzerhof (PBE) [31] formulation of the generalized gradient approximation (GGA). The ion-electron interactions were represented by the projector augmented wave (PAW) [32] method. A plane-wave basis set with an energy cutoff of 400 eV was used. The k-point sampling was performed using the Monkhorst–Pack scheme [33]. The electronic self-consistent minimization was converged to 10^{-5} eV, and the geometry optimization was converged to -0.02 eV. The lattice constants of HAP were optimized to be $a = b = 9.424$ Å and $c = 6.879$. Å. We used them to build a (1×1) (001) slab. A $4 \times 4 \times 1$ k-point mesh was used. Four Pt atoms were used to show the Pt nanoparticle loaded on HAP (001). The work functions were calculated using HAP (001) and Pt (111).

3. Results and discussions

3.1. Crystal structure and chemical compositions

The Pt/HAP was prepared via an impregnation method. H_2PtCl_6 was impregnated on HAP, followed by reduction at 400 °C under H_2 atmosphere. The crystal structures of the samples were characterized by X-ray diffraction (XRD). All diffraction peaks are in good agreement with hexagonal phase HAP (JCPDS card NO. 09-0432) (Fig. 1a). No diffraction peaks assigned to Pt are observed on Pt/HAP, which is due to its low content and high dispersity [34]. X-ray photoelectron spectroscopy (XPS) was conducted to investigate the valence states and surface elemental composition of Pt/HAP. The survey scan spectrum of Pt/HAP reveals the presence of Ca, O, P, and Pt elements (Fig. S1a). The Pt 4 f signal could be deconvoluted into two peaks located at 70.9 eV and 74.3 eV, which are assigned to 4 $f_{7/2}$ and 4 $f_{5/2}$ of Pt^0 (Fig. 1b) [35].
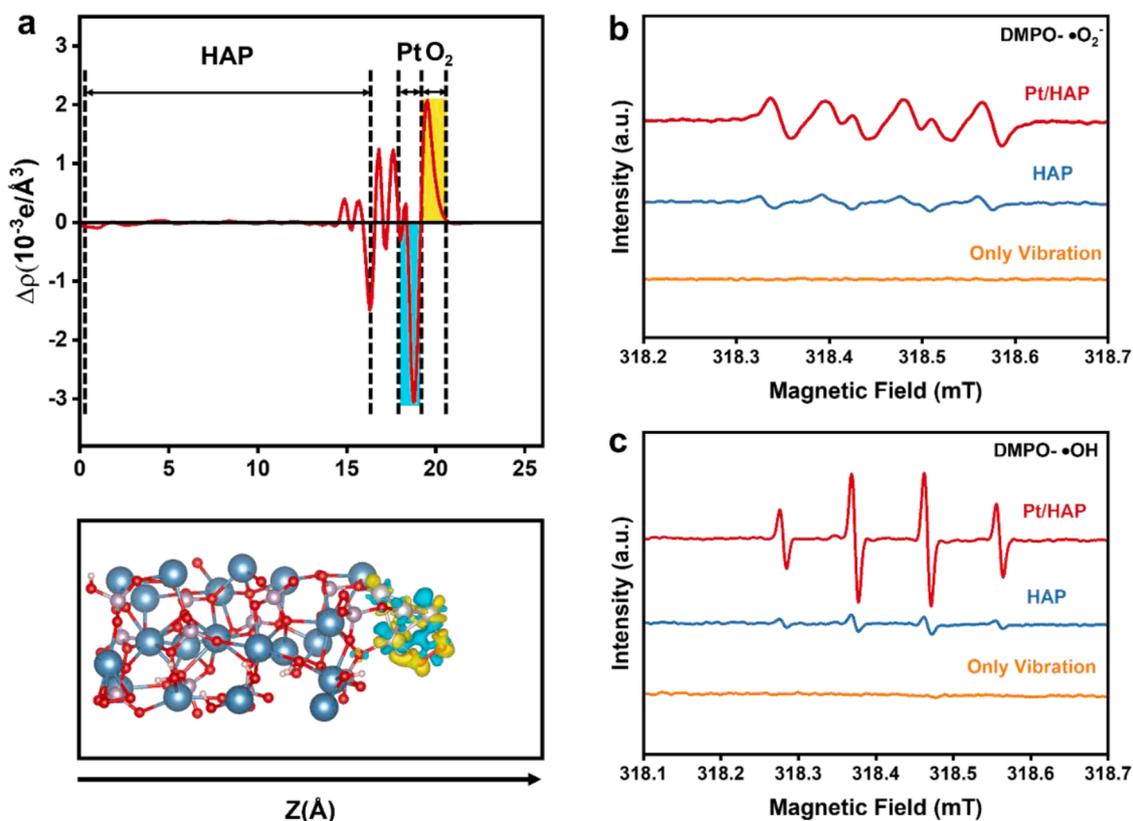
Fig. 5. (a) Charge density difference diagram of Pt/HAP with the adsorption of O_2 molecule. (The yellow and cyan area represents electron accumulation and depletion, respectively) (b) ESR spectra of DMPO-•O_2^- in methanol. (c) ESR spectra of DMPO-•OH in water.

Compared with pristine HAP, the peaks of O 1 s, Ca 2p and P 2p shift towards lower binding energy due to the strong interaction between Pt and HAP (Fig. S1b-d) [36]. As shown by the high-resolution transmission electron microscope (HRTEM), Pt nanoparticles with a size of 5–10 nm are dispersed on HAP support, and the lattice space of the Pt (111) plane is observed (Fig. 1c) [37]. Element mapping spectra further shows that Pt is homogeneously distributed on the surface of HAP (Fig. 1d). The intimate contact between Pt and HAP could be favorable for the migration of piezo-induced charges.

3.2. PFM characterizations

Piezoelectric force microscopy (PFM) was carried out to investigate the piezoelectric properties of the Pt/HAP. A coarse surface with bright spots can be seen in the topography image owing to the decoration of Pt (Fig. 2a) [38]. The signal disturbance of Pt nanoparticles further affects the contrasts in the amplitude and phase images (Fig. 2b and c). The amplitude–voltage butterfly loop and phase–voltage hysteresis loop reveal the excellent piezoelectric nature of Pt/HAP (Fig. 2d, Fig. S2a-d), whose maximum amplitudes could reach about 350 pm.

3.3. Piezoelectrical charges properties

The photoelectric behavior of the samples was further studied. UV–vis diffuse reflectance spectra (DRS) reveal the broadening of absorption range and the color of catalysts turned brown from white (Fig. 2a). To analyze the energy band structure of catalysts, Mott-Schottky plots were carried out to determine the position of the flat band (Fig. 2b). The positive slopes of curves revealed typical n-type semiconductor properties. The flat-band potentials of HAP and Pt/HAP were estimated to be − 0.83 V and − 0.94 V. The conduction band (CB) position was more negative about 0.2 V than the flat band potential for most n-type semiconductors [39]. Therefore, the CB of HAP and Pt/HAP

were estimated to be − 0.63 V and − 0.74 V (Fig. S3, Table S1) [40]. Open-circuit voltage decay (OCVD) was conducted to investigate carrier dynamics (Fig. 2c). A piezo-induced voltage decrease was evidenced under vibration. The average lifetime for Pt/HAP, especially the long-lived distribution ($\tau > 100$ s, black double-headed arrow), is longer than that of pristine HAP (Fig. 2d), indicating an improved carrier dynamic [41]. The immobilization of Pt on HAP promotes piezo-induced carrier separation as demonstrated by the piezocurrent and electrochemical impedance spectroscopy (EIS) characterizations. Compared with pure HAP, Pt/HAP exhibits a stronger piezocurrent signal (Fig. 2e). EIS reveals that Pt/HAP owns less charge transfer resistance (Fig. 2f). The decoration of Pt on HAP significantly promotes the separation and migration of charge carriers.

3.4. Piezocatalytic oxidation

We then performed the piezocatalytic HMF oxidation under vibration (20 kHz) in H_2O solvent and air atmosphere (Fig. 4a, Fig. S4). Most of the widely used catalysts, such as Bi_2WO_6, $Bi_4Ti_3O_{12}$, $BiOIO_3$ were inactive for this reaction. HAP showed low activity with 1% yield of FFCA, while the immobilization of metals could enhance piezocatalytic activity (Fig. S5). Pt/HAP shows the best performance with 96% HMF conversion and 70% FFCA yield in 2 h. A comparison of HMF oxidation to FFCA of different catalysts was shown in Table S2 [42–45]. The atmosphere shows a significant effect on HMF oxidation. The replacement of air with argon significantly decreases the reaction activity, indicating the oxidation is majorly conducted by oxygen (Fig. S6). Besides, blank experiments reveal that ultrasonic-induced stress plays a key role in the catalytic oxidation reaction, and only 17% yield of FFCA was obtained without ultrasonic vibration (Fig. S7).

There are two possible pathways for the oxidation of HMF to FFCA. In path 1, the hydroxylic group of HMF is first oxidized to afford DFF and then further oxidized to FFCA. In path 2, the aldehydic group of HMF is
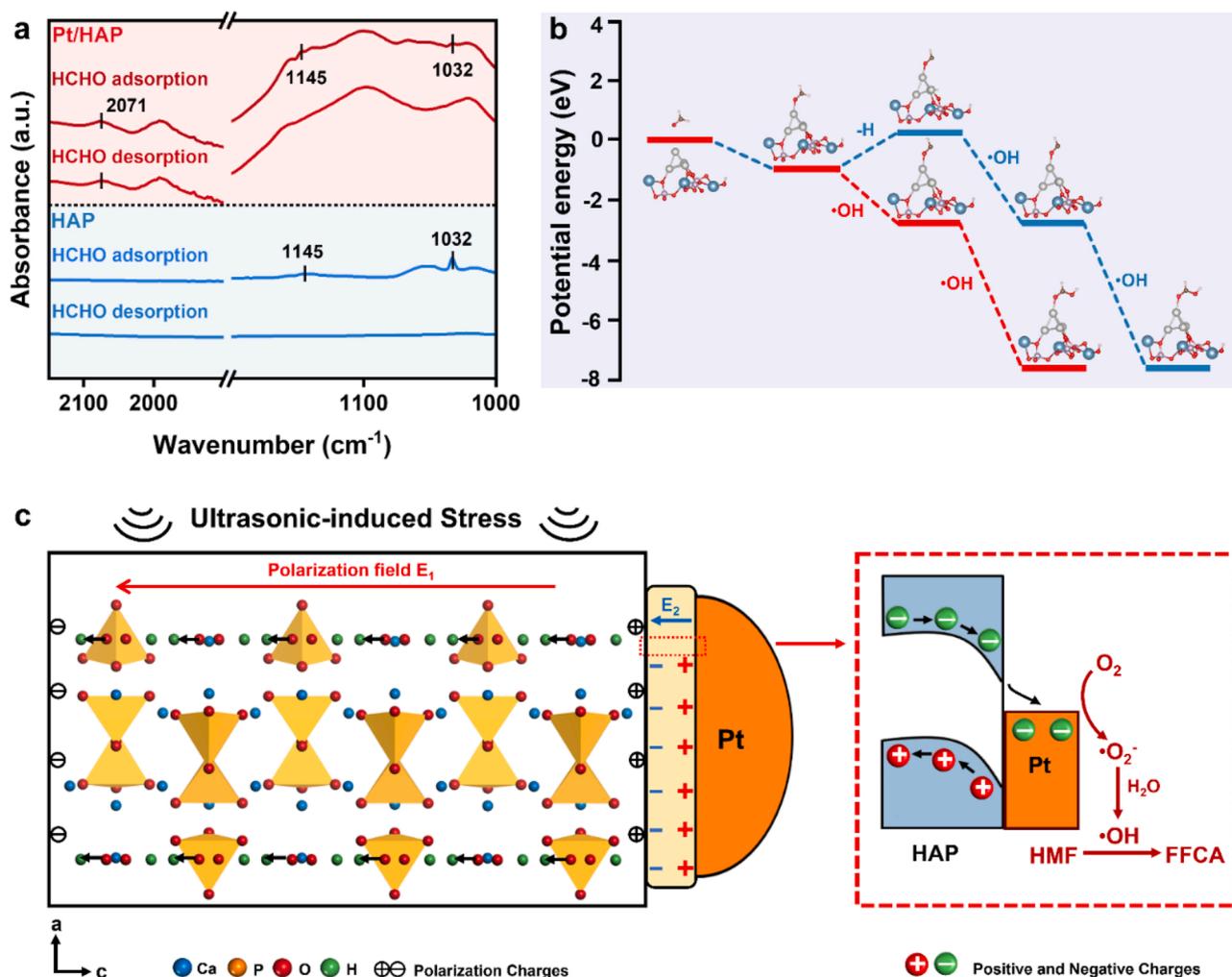
Fig. 6. (a) FTIR spectra for HCHO absorption over HAP and Pt/HAP. (b) DFT calculation for the conversion of formaldehyde to formic acid over Pt/HAP. (c) Schematic diagram of the piezocatalytic HMF oxidation process over Pt/HAP.

first oxidized to afford HMFCA, which is then further oxidized to FFCA. The time curves of HMF oxidation over Pt/HAP were recorded to explore the reaction route in this piezocatalytic system (Fig. 3b). Notably, no DFF intermediate was detected. HMFCA is detected and its concentration was first increased to a maximum and then decreased, implying piezocatalytic HMF oxidation probably undergoes path 2 (Fig. 3c). Pt/HAP was stable under the reaction conditions and could be reused four times without dramatic decrease (Fig. S8a-b). The slight activity decrease could be ascribed to the mass loss during the recycling of the catalyst. To demonstrate the feasibility of this piezocatalytic approach, we further investigated the oxidation of other aldehydes and alcohols. Fatty aldehydes, furan aldehydes, fatty alcohols, and ethylene glycol could all be oxidized to the corresponding carboxylic acids with 58–96% conversion and 43–84% yield (Table 1 and Fig. S9-S17).
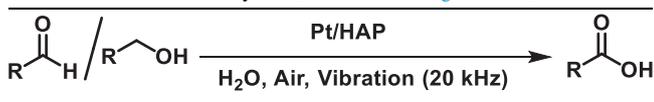
3.5. Reactive oxygen species (ROS) generation

Density functional theory (DFT) is performed to further investigate the activation of O_2 (Fig. 5a). The charge density difference of Pt/HAP reveals that Pt could effectively activate O_2 molecule, which was beneficial for the generation of reactive oxygen species [46,47]. The reaction mechanism was studied using trapping experiment and in situ electron spin resonance (ESR) using dimethyl pyridine N-oxide (DMPO) as a spin-trapping reagent [48]. The addition of radical-trapping reagent 4-benzoquinone (BZQ) and isopropanol (IPA) significantly suppressed HMF oxidation, indicating the importance of $\bullet O_2^-$ and $\bullet OH$ radical for this piezocatalytic progress (Fig. S18) [49]. Two characteristic signals, which correspond to superoxide radical ($\bullet O_2^-$) and hydroxyl radical ($\bullet OH$), can be observed under vibration (Fig. 5b and c). The $\bullet OH$ radical is derived from the reduction of oxygen by the piezo-induced electrons [50]. Pt/HAP exhibits a stronger radical signal due to improved charge separation efficiency and the activation of oxygen by Pt.

3.6. Piezocatalytic oxidation mechanism

The adsorption of the substrate on the surface plays a key role in the catalytic oxidation reaction. We then investigated the adsorptive Fourier transform infrared spectrometer (FTIR) using formaldehyde as the probe molecule (Fig. 6a). After the introduction of formaldehyde vapor, formaldehyde molecule peaks at 1145 and 1032 cm^{-1} were observed on HAP [51]. These peaks disappeared after evacuation, indicating the weak interaction on pristine HAP. In contrast, the peak at 2071 cm^{-1}, which is assigned to the adsorption of carbonyl groups on Pt sites [52], was still reserved on Pt/HAP after desorption. These results reveal that the immobilization of Pt on HAP could enhance the adsorption of the aldehyde group (-CHO) of the substrates.

We further studied the oxidation progress of the aldehyde group using formaldehyde as the probe molecule by DFT calculation (Fig. 6b).

Firstly, formaldehyde was closely adsorbed on Pt/HAP surface with C═O binding to Pt ($E_{ads} = -0.96$ eV) as demonstrated by the adsorptive FTIR characterization. The C-H bond cleavage was a rate-determining step and can be cleaved via hydrogen transfer to Pt or directly reacting with •OH radical. The direct hydrogen abstraction by •OH is thermodynamically more favorable with reaction energy of -1.61 eV, while hydrogen transfer to Pt is endothermal. Finally, the formyl is easily combined with •OH radical to form formic acid with a large negative reaction energy (-4.83 eV).

Based on the above results, a possible piezocatalytic mechanism of HMF oxidation was proposed (Fig. 6c). Hexagonal ($P6_3/m$) HAP, whose piezoelectricity is ascribed to the polarization of OH^- groups confined to the channel formed by the overlapping hexagonal calcium atoms, could generate a spontaneous ferroelectric polarization. The hydrogen and the oxygen atoms are equally distributed along [001] direction and provide a paraelectric arrangement of O and H atoms [53]. The ferroelectric polarization of HAP provides a giant piezoelectric field (E_1) for separating piezo-generated charges. The work function of the HAP is larger than that of Pt (Fig. S19a-b). As demonstrated by the charge density difference (Fig. S18c), when Pt is loaded on HAP, the electrons will transfer from Pt to HAP, thus forming an electric field (E_2). The direction of this surface electric field is the same as the bulk nonlocal piezoelectric field of HAP, which greatly promotes the charges separation and migration from bulk to the Pt. When subjected to mechanical vibration, the electrons will smoothly migrate from bulk to Pt driven by coupling E_1 and E_2 electron fields. Activated molecular oxygen on Pt was thus reduced by the electrons to generate •O_2^- radical, which is further converted to •OH radical. These active oxygen species oxidize HMF to FFCA.

4. Conclusion

In summary, we reported a novel piezocatalytic method for the selective oxidation HMF to FFCA. Pt/HAP is effective for piezocatalytic HMF oxidation reaction. The immobilization of Pt on HAP greatly promotes the separation and migration of charges from bulk to Pt due to the coupling of nonlocal piezoelectric field and localized surface electric field. Pt also enhances the adsorption and activation of O_2 molecules and organic substrates. We believe this work will endow new inspirations on utilizing mechanical energy to produce value-added chemicals from biomass.

CRediT authorship contribution statement

Zhiwei Chen: Conducted most of the experiments in this work, Analyzed the data. **Hongru Zhou, Fanhao Kong**: Performed the catalyst characterization. **Min Wang, Zhiwei Chen**: Cowrote the manuscript. **Min Wang**: Conceived and supervised the research and revised the manuscript.

Declaration of Competing Interest

The authors declare that they have no known competing financial interests or personal relationships that could have appeared to influence the work reported in this paper.

Acknowledgments

Conflict of Interest

The authors declare no conflict of interest.

Appendix A. Supporting information

Supplementary data associated with this article can be found in the online version at doi:10.1016/j.apcatb.2022.121281.

References

[1] N. Luo, T. Montini, J. Zhang, P. Fornasiero, E. Fonda, T. Hou, W. Nie, J. Lu, J. Liu, M. Heggen, L. Lin, C. Ma, M. Wang, F. Fan, S. Jin, F. Wang, Visible-light-driven coproduction of diesel precursors and hydrogen from lignocellulose-derived methylfurans, Nat. Energy 4 (2019) 575–584.

[2] Z. Huang, Z. Zhao, C. Zhang, J. Lu, H. Liu, N. Luo, J. Zhang, F. Wang, Enhanced photocatalytic alkane production from fatty acid decarboxylation via inhibition of radical oligomerization, Nat. Catal. 3 (2020) 170–178.

[3] M. Wang, F. Wang, Catalytic scissoring of lignin into aryl monomers, Adv. Mater. 31 (2019) 1901866.

[4] M. Wang, J. Ma, H. Liu, N. Luo, Z. Zhao, F. Wang, Sustainable productions of organic acids and their derivatives from biomass via selective oxidative cleavage of C–C bond, ACS Catal. 8 (2018) 2129–2165.

[5] M. Wang, M. Liu, J. Lu, F. Wang, Photo splitting of bio-polyols and sugars to methanol and syngas, Nat. Commun. 11 (2020) 1083.

[6] H.R. Zhou, M. Wang, F. Wang, Oxygen-vacancy-mediated catalytic methanation of lignocellulose at temperatures below 200 °C, Joule 5 (2021) 3031–3044.

[7] F.H. Kong, M. Wang, Preparation of sulfur-modulated nickel/carbon composites from lignosulfonate for the electrocatalytic oxidation of 5-hydroxymethylfurfural to 2,5-furandicarboxylic acid, ACS Appl. Energy Mater. 4 (2021) 1182–1188.

[8] T. Wang, L. Tao, X. Zhu, C. Chen, W. Chen, S. Du, Y. Zhou, B. Zhou, D. Wang, C. Xie, P. Long, W. Li, Y. Wang, R. Chen, Y. Zou, X.Z. Fu, Y. Li, X. Duan, S. Wang, Combined anodic and cathodic hydrogen production from aldehyde oxidation and hydrogen evolution reaction, Nat. Catal. 5 (2021) 66–73.

[9] G. Wang, R. Huang, J. Zhang, J. Mao, D. Wang, Y. Li, Synergistic modulation of the separation of photo-generated carries via engineering of dual atomic sites for promoting photocatalytic performance, Adv. Mater. (2021) 2105904, https://doi.org/10.1002/adma.202105904.

[10] Y. Lu, T. Liu, C.L. Dong, C. Yang, L. Zhou, Y.C. Huang, Y. Li, B. Zhou, Y. Zou, S. Wang, Tailoring competitive adsorption sites by oxygen-vacancy on cobalt oxides to enhance the electrooxidation of biomass, Adv. Mater. (2021), e2107185, https://doi.org/10.1002/adma.202107185.

[11] S. Xu, P. Zhou, Z. Zhang, C. Yang, B. Zhang, K. Deng, S. Bottle, H. Zhu, Selective oxidation of 5-hydroxymethylfurfural to 2,5-furandicarboxylic acid using O_2 and a photocatalyst of co-thioporphyrazine bonded to g-C_3N_4, J. Am. Chem. Soc. 139 (2017) 14775–14782.

[12] Z. Zhang, G.W. Huber, Catalytic oxidation of carbohydrates into organic acids and furan chemicals, Chem. Soc. Rev. 47 (2018) 1351–1390.

[13] I. Delidovich, P.J. Hausoul, L. Deng, R. Pfutzenreuter, M. Rose, R. Palkovits, Alternative monomers based on lignocellulose and their use for polymer production, Chem. Rev. 116 (2016) 1540–1599.

[14] M. Ventura, M. Aresta, A. Dibenedetto, Selective aerobic oxidation of 5-(hydroxymethyl)furfural to 5-formyl-2-furancarboxylic acid in water, ChemSusChem 9 (2016) 1096–1100.

[15] Y.Z. Qin, Y.M. Li, M.H. Zong, H. Wu, N. Li, Enzyme-catalyzed selective oxidation of 5-hydroxymethylfurfural (HMF) and separation of HMF and 2,5-diformylfuran using deep eutectic solvents, Green Chem. 17 (2015) 3718–3722.

[16] Y. Wang, Y. Xu, S. Dong, P. Wang, W. Chen, Z. Lu, D. Ye, B. Pan, D. Wu, C. D. Vecitis, G. Gao, Ultrasonic activation of inert poly(tetrafluoroethylene) enables piezocatalytic generation of reactive oxygen species, Nat. Commun. 12 (2021) 3508.

[17] J. Ma, J. Ren, Y. Jia, Z. Wu, L. Chen, N.O. Haugen, H. Huang, Y. Liu, High efficiency bi-harvesting light/vibration energy using piezoelectric zinc oxide nanorods for dye decomposition, Nano Energy 62 (2019) 376–383.

[18] R. Su, H.A. Hsain, M. Wu, D. Zhang, X. Hu, Z. Wang, X. Wang, F.T. Li, X. Chen, L. Zhu, Y. Yang, Y. Yang, X. Lou, S.J. Pennycook, Nano-ferroelectric for high efficiency overall water splitting under ultrasonic vibration, Angew. Chem. Int. Ed. 58 (2019) 15076–15081.

[19] A. Zhang, Z.Y. Liu, B. Xie, J.S. Lu, K. Guo, S.M. Ke, L.L. Shu, H.Q. Fan, Vibration catalysis of eco-friendly $Na_{0.5}K_{0.5}NbO_3$-based piezoelectric: an efficient phase boundary catalyst, Appl. Catal. B Environ. 279 (2020), 119353.

[20] N. Zhao, Y. Feng, H.J. Zhao, H.Q. Fan, S. Tian, B.B. Hu, Simple electrodeposition of 3D NiCoFe-layered double hydroxide nanosheet assembled nanospheres/nanoflowers on carbon cloth for high performance hybrid supercapacitors, J. Alloy. Compd. 901 (2022), 163566.

[21] N. Zhao, H.Q. Fan, M.C. Zhang, C. Wang, X.H. Ren, H.J. Peng, H. Li, X.B. Jiang, X. Q. Cao, Preparation of partially-cladding NiCo-LDH/Mn_3O_4 composite by electrodeposition route and its excellent supercapacitor performance, J. Alloy. Compd. 796 (2019) 111–119.

[22] S. Song, S. Qu, P. Han, M.J. Hulsey, G. Zhang, Y. Wang, S. Wang, D. Chen, J. Lu, N. Yan, Visible-light-driven amino acids production from biomass-based feedstocks over ultrathin CdS nanosheets, Nat. Commun. 11 (2020) 4899.

[23] M. Wang, B. Wang, F. Huang, Z. Lin, Enabling piezo-potential in piezoelectric semiconductors for enhanced catalytic activities, Angew. Chem. Int. Ed. 58 (2019) 7526–7536.

[24] J.M. Wu, W.E. Chang, Y.T. Chang, C.K. Chang, Piezo-catalytic effect on the enhancement of the ultra-high degradation activity in the dark by single- and few-layers MoS_2 nanoflowers, Adv. Mater. 28 (2016) 3718–3725.

[25] H. You, H. You, Z. Wu, L. Zhang, Y. Ying, Y. Liu, L. Fei, X. Chen, Y. Jia, Y. Wang, F. Wang, S. Ju, J. Qiao, C.H. Lam, H. Huang, Harvesting the vibration energy of $BiFeO_3$ nanosheets for hydrogen evolution, Angew. Chem. Int. Ed. 58 (2019) 11779–11784.

[26] L. Lei, W.J. Wang, C. Wang, H.Q. Fan, A.K. Yadav, N. Hu, Q. Zhong, P. M. Buschbaum, Hydrogel-supported graphitic carbon nitride nanosheets loaded with Pt atoms as a novel self-water-storage photocatalyst for H_2 evolution, J. Mater. Chem. A 8 (2020) 23812–23819.

[27] Y. Zhou, H. Wang, X. Liu, S. Qiao, D. Shao, J. Zhou, L. Zhang, W. Wang, Direct piezocatalytic conversion of methane into alcohols over hydroxyapatite, Nano Energy 79 (2021).

[28] Z.Y. Wang, H.Q. Fan, K.H. Su, Z.Y. Wen, Structure and piezoelectric properties of poly(vinylidene fluoride) studied by density functional theory, Polymer 47 (2006) 7988–7996.

[29] W.J. Wang, H.Q. Fan, Y.X. Ye, Effect of electric field on the structure and piezoelectric properties of poly(vinylidene fluoride) studied by density functional theory, Polymer 51 (2010) 3575–3581.

[30] G. Kresse, J. Furthmuller, Efficiency of ab-initio total energy calculations for metals and semiconductors using a plane-wave basis set, Comput. Mater. Sci. 6 (1996) 15–50.

[31] J.P. Perdew, K. Burke, M. Ernzerhof, Generalized gradient approximation made simple, Phys. Rev. Lett. 77 (1996) 3865–3868.

[32] G. Kresse, D. Joubert, From ultrasoft pseudopotentials to the projector augmented-wave method, Phys. Rev. B 59 (1999) 1758–1775.

[33] H.J. Monkhorst, J.D. Pack, Special points for brillouin-zone integrations, Phys. Rev. B 13 (1976) 5188–5192.

[34] X.N. Ren, Z.Y. Hu, J. Jin, L. Wu, C. Wang, J. Liu, F. Liu, M. Wu, Y. Li, G. V. Tendeloo, B.L. Su, Cocatalyzing Pt/PtO phase-junction nanodots on hierarchically porous TiO_2 for highly enhanced photocatalytic hydrogen production, ACS Appl. Mater. Interfaces 9 (2017) 29687–29698.

[35] Z. Zhang, J. Zhen, B. Liu, K. Lv, K. Deng, Selective aerobic oxidation of the biomass-derived precursor 5-hydroxymethylfurfural to 2,5-furandicarboxylic acid under mild conditions over a magnetic palladium nanocatalyst, Green Chem. 17 (2015) 1308–1317.

[36] Z. Boukha, J.R. González-Velasco, M.A. Gutiérrez-Ortiz, Platinum supported on lanthana-modified hydroxyapatite samples for realistic WGS conditions: on the nature of the active species, kinetic aspects and the resistance to shut-down/start-up cycles, Appl. Catal. B Environ. 270 (2020).

[37] Y. Kang, M. Li, Y. Cai, M. Cargnello, R.E. Diaz, T.R. Gordon, N.L. Wieder, R. R. Adzic, R.J. Gorte, E.A. Stach, C.B. Murray, Heterogeneous catalysts need not be so "heterogeneous": monodisperse Pt nanocrystals by combining shape-controlled synthesis and purification by colloidal recrystallization, J. Am. Chem. Soc. 7 (2013) 2741–2747.

[38] G. Yang, Q. Chen, W. Wang, S. Wu, B. Gao, Y. Xu, Z. Chen, S. Zhong, J. Chen, S. Bai, Cocatalyst engineering in piezocatalysis: a promising strategy for boosting hydrogen evolution, ACS Appl. Mater. Interfaces 13 (2021) 15305–15314.

[39] C. Zeng, Y. Hu, F. Dong, X. Du, Achieving tunable photocatalytic activity enhancement by elaborately engineering composition-adjustable polynary heterojunctions photocatalysts, Appl. Catal. B Environ. 194 (2017) 62–73.

[40] Z. Zhang, M. Wang, H. Zhou, F. Wang, Surface sulfate ion on CdS catalyst enhances syngas generation from biopolyols, J. Am. Chem. Soc. 143 (2021) 6533–6541.

[41] C. Huang, S. Zou, Y. Liu, S. Zhang, Q. Jiang, T. Zhou, S. Xin, J. Hu, Surface reconstruction-associated partially amorphized bismuth oxychloride for boosted photocatalytic water oxidation, ACS Appl. Mater. Interfaces 13 (2021) 5088–5098.

[42] M. Ventura, F. Lobefaro, E. Giglio, M. Distaso, F. Nocito, A. Dibenedetto, Selective aerobic oxidation of 5-hydroxymethylfurfural to 2,5-diformylfuran or 2-formyl-5-furancarboxylic acid in water by using $MgO \bullet CeO_2$ mixed oxides as catalysts, ChemSusChem 11 (2018) 1305–1315.

[43] P. Pal, S. Kumar, M.M. Devi, S. Saravanamurugan, Oxidation of 5-hydroxyme-thylfurfural to 5-formyl furan-2-carboxylic acid by non-precious transition metal oxide-based catalyst, J. Supercrit. Fluid 160 (2020), 104812.

[44] C. Zhang, X. Chang, L. Zhu, Q.G. Xing, S.P. You, W. Qi, R.X. Su, Z.M. He, Highly efficient and selective production of FFCA from CotA-TJ102 laccase-catalyzed oxidation of 5-HMF, Int. J. Biol. Macromol. 128 (2019) 132–139.

[45] Y.K. Zhu, Y. Zhang, L.L. Cheng, M. Ismael, Z.Y. Feng, Y. Wu, Novel application of g-C_3N_4/$NaNbO_3$ composite for photocatalytic selective oxidation of biomass-derived HMF to FFCA under visible light irradiation, Adv. Powder Technol. 31 (2020) 1148–1159.

[46] Y. Liu, H.Y. Ma, D. Lei, L.L. Lou, S. Liu, W. Zhou, G.C. Wang, K. Yu, Active oxygen species promoted catalytic oxidation of 5-Hydroxymethyl-2-furfural on facet-specific Pt nanocrystals, ACS Catal. 9 (2019) 8306–8315.

[47] H.R. Zhou, M. Wang, F. Wang, Oxygen-controlled photo-reforming of biopolyols to CO over Z-scheme CdS@g-C_3N_4, Chem (2021), https://doi.org/10.1016/j.chempr.2021.10.021.

[48] S. Xie, Z. Shen, J. Deng, P. Guo, Q. Zhang, H. Zhang, C. Ma, Z. Jiang, J. Cheng, D. Deng, Y. Wang, Visible light-driven C–H activation and C–C coupling of methanol into ethylene glycol, Nat. Commun. 9 (2018) 1181.

[49] Z. Chen, C. Huang, T. Zhou, J. Hu, Strike a balance between adsorption and catalysis capabilities in $Bi_2Se_{3-x}O_x$ composites for high-efficiency antibiotics remediation, Chem. Eng. J. 382 (2020), 122877.

[50] Y. Nosaka, A.Y. Nosaka, Generation and detection of reactive oxygen species in photocatalysis, Chem. Rev. 117 (2017) 11302–11336.

[51] X. Yang, X. Yu, M. Lin, M. Ge, Y. Zhao, F. Wang, Interface effect of mixed phase Pt/ZrO_2 catalysts for HCHO oxidation at ambient temperature, J. Mater. Chem. A 5 (2017) 13799–13806.

[52] S. Lei, S. Qin, B. Li, C. Zhao, Pt/HAP catalyzed direct decarboxylation of lipid to alkanes via stabilization and synergism effect, J. Catal. 400 (2021) 244–254.

[53] S.B. Hu, F.H. Jia, C. Marinescu, F. Cimpoesu, Y.T. Qi, Y.X. Tao, A. Stroppa, W. Ren, Ferroelectric polarization of hydroxyapatite from density functional theory, RSC Adv. 7 (2017) 21375–21379.